

The Rise of Nova V1674 Herculis

ROBERT M. QUIMBY ^{1,2} BRIAN D. METZGER ^{3,4} KEN J. SHEN ⁵ ALLEN W. SHAFER ¹ HANK CORBETT ⁶ AND
MADELINE OVERTON⁷

¹*Department of Astronomy and Mount Laguna Observatory
San Diego State University, San Diego, CA 92182, USA*

²*Kavli Institute for the Physics and Mathematics of the Universe (WPI)
The University of Tokyo Institutes for Advanced Study
The University of Tokyo, Kashiwa, Chiba 277-8583, Japan*

³*Department of Physics and Columbia Astrophysics Laboratory, Columbia University, New York, NY 10027, USA*

⁴*Center for Computational Astrophysics, Flatiron Institute, 162 5th Ave, New York, NY 10010, USA*

⁵*Department of Astronomy and Theoretical Astrophysics Center, University of California, Berkeley, CA 94720, USA*

⁶*Department of Physics & Astronomy
University of North Carolina at Chapel Hill, Chapel Hill, NC 27514, USA*

⁷*Department of Physics and Astronomy and Nevada Center for Astrophysics, University of Nevada, Las Vegas, 4505 South Maryland
Parkway, Las Vegas, NV 89154, USA*

ABSTRACT

Observational constraints on classical novae are heavily biased to phases near optical peak and later because of the simple fact that novae are not typically discovered until they become bright. The earliest phases of brightening, coming before discovery, are typically missed, but this is changing with the proliferation of wide-field optical monitoring systems including ZTF, ASAS-SN, and Evryscope. Here, we report on unprecedented observations of the fast nova V1674 Her beginning >10 mag below its optical peak and including high-cadence (2 min.) observations that chart a rise of ~ 8 mag in just 5 hours. Two clear breaks are identified as the light curve transitions first from rising slowly to rising rapidly, followed by a transition to an even faster, nearly linear rate of increasing flux with time. The depths of the observations allow us to place tight constraints on the size of the photosphere under the assumption of blackbody emission from a white dwarf emitting at its Eddington luminosity. We find that the white dwarf was unlikely to have overflowed its Roche lobe prior to the launch of a fast wind, which poses a challenge for explaining the Fermi γ -ray detections as the interaction of a fast wind with a slow-torus of gas stripped from the inflated white dwarf envelope by the companion. High-cadence observations of novae from Evryscope and the planned Argus Array can record the diversity of rising nova light curves and help resolve how the interplay between thermonuclear fusion, binary interaction, and shocks power their earliest light.

Keywords: Classical Novae (251)

1. INTRODUCTION

Classical novae, non-terminal outbursts that occur when the envelope accreted onto a white dwarf (WD) star ignites (see Chomiuk et al. 2021 for a review), are typically discovered near peak optical brightness¹. Follow-up campaigns can be initiated soon thereafter to record the evolution of the nova in detail as it fades, but the rising portion of the light curve is typically poorly

constrained, especially for the most rapidly evolving novae (e.g., see examples in Strobe et al. 2010).

In most cases the nova is first detected when it is within 2 mag of its optical peak, which, by definition of a nova, means that at least the first 6 mag of brightening are missed. Some novae have historical imaging that provides detections of the progenitor systems in quiescence prior to outburst (Schaefer 2021), but almost all lack a detailed record of how the nova transitioned from its quiescent state to outburst. Notable exceptions include observations of RS Oph, V598 Pup, and KT Eri starting ~ 4 mag below peak with the Solar Mass

¹ For a listing of nova discovery and peak magnitudes, see <https://github.com/Bill-Gray/galnovae/blob/master/galnovae.txt>

Ejection Imager (Hounsell et al. 2010), observations of the very slow Nova Velorum 2022 (Gaia22alz) starting ~ 7 mag below peak (Aydi et al. 2023), observations of ASASSN-16ma starting ~ 8 mag below peak (Li et al. 2017), and observations of T Pyxidis, whose 2011 outburst was discovered and then intensively followed up starting ~ 8 mag below peak (Schaefer et al. 2013). In this study we discuss the unprecedented >10 mag rise of Nova Herculis 2021 (V1674 Her) and how its early light curve can be used to constrain the initial expansion phases of the outburst.

Novae were once thought to be powered exclusively by the radiation emitted by thermonuclear fusion at the base of the accreted envelope (Gallagher & Starfield 1978), but the shocking discovery of γ -ray novae has forced a revision of the theory (Ackermann et al. 2014). Observational evidence still shows that nova systems contain a white dwarf interacting with its companion (Patterson 1984), and thus it is believed that stable accretion onto the WD builds an envelope of fuel until the rate of energy generated by thermonuclear fusion exceeds the rate this energy can diffuse away (e.g., Prialnik et al. 1979). This is often described as “thermonuclear runaway” in the literature, but we emphasize that there can be a long simmering phase prior to the convective zone reaching the photosphere. It is at this point the luminosity of the WD photosphere begins to increase, but initially the radius of the WD remains essentially constant. As the luminosity approaches the Eddington limit, the WD envelope begins to expand and the temperature drops accordingly to maintain the Eddington luminosity. The increasing radius and lowering temperature conspire to produce a rise in optical flux. When the photospheric temperature drops to roughly 1.5×10^5 K, the opacity increases due to Fe-peak elements, and a fast, optically thick wind may be launched (Kato & Hachisu 1994). However, this temperature transition may occur at around the time the WD fills its own Roche lobe, which means the companion may be important to what follows (Shen & Quataert 2022).

One possibility is that once the WD fills its Roche lobe material begins flowing to the companion, which, having already filled its own Roche lobe, cannot accrete further material. Thus the extra material ends up ejected from the L2 nozzle opposite the companion from the WD and a torus of gas forms in the equatorial plane of the system (e.g., Pejcha et al. 2016; Lu et al. 2023). This scenario is supported by high-resolution radio imaging (e.g., Chomiuk et al. 2014) and spectroscopic observations of nova outbursts that show P-Cygni profiles prior to maximum light with absorption troughs blue shifted by velocities consistent with the orbital velocities of the binary

(Aydi et al. 2020a). When the fast wind is launched, it may interact with this relatively slow-moving torus to produce γ -ray emission as well as optical light (Metzger et al. 2014; Li et al. 2017; Munari et al. 2017; Aydi et al. 2020b). Nova spectra taken after maximum light have shown multiple velocity components that can be identified as the slow torus, the fast wind, and intermediate-width features that can be identified as the interaction region of these two.

A white dwarf filling its Roche lobe and emitting at its Eddington luminosity will have an absolute g -band magnitude in the optical of $M_g \sim -1$, which is ~ 6 mag below the typical peak of novae. As mentioned, novae are not typically discovered until they are much brighter in the optical, so there is a lack of direct observational data documenting potential interactions between the WD and its companion at this phase. The rise of wide field optical transient surveys is, however, changing this picture. The Zwicky Transient Facility (ZTF; Bellm et al. 2019; Graham et al. 2019), the All-Sky Automated Survey for Supernovae (ASAS-SN; Shappee et al. 2014; Kochanek et al. 2017, and others now routinely capture snapshots of large swaths of sky each night. These surveys do not always first identify novae at young phases because of the candidate vetting process, but the images are archived and can be mined after discovery. Evryscope takes wide field monitoring a step further by obtaining not just snapshots but nightly movies built from hundreds of exposures covering thousands of square degrees simultaneously (Law et al. 2014). These surveys operate at depths sufficient to detect the earliest evolutionary phases of galactic novae.

V1674 Her has been the subject of multiple studies (e.g., Woodward et al. 2021a; Drake et al. 2021; Patterson et al. 2022; Sokolovsky et al. 2023; Bhargava et al. 2024; Hattie et al. 2024) due to several unique factors: 1) with a peak apparent magnitude of $V \sim 6.2$ (see Appendix A), it is among the top 5% brightest novae found this century; 2) the visual decline of 2 magnitudes from peak in just 1 day makes it perhaps the fastest novae on record; 3) extensive pre-outburst imaging of the progenitor system by ZTF place tight constraints on the white dwarf spin period prior to outburst (Mroz et al. 2021); 4) Fermi detected a coincident γ -ray source that turned on during the optical peak (Sokolovsky et al. 2023); and 5) periodicity was detected in the X-Ray and optical light curves just two weeks after the optical peak that reveal the orbital period (Patterson et al. 2022). In this paper we focus on another remarkable aspect of V1674 Her: pre-discovery images from ASAS-SN and Evryscope that begin with the nova 10 magnitudes below its optical peak and capture a gradual brighten-

ing phase, a quick transition to a fast rise, and a second transition to an even faster rise.

We discuss some of the key observational constraints of the V1674 Her system in §2 and provide estimates for the scale of the system in §2.1. In §3 we present new analysis of pre-discovery optical photometry from ASAS-SN and Evryscope including discussion of a process we dub “image model subtraction” that we use to extract photometry from the crowded Evryscope images (§3.2.1). We analyze the rising light curve in §4, and construct simple models in §5 to help interpret these data. Discussion and conclusions are offered in §6. For convenience, we adopt an agnostic reference epoch, t_{ref} , of HJD 2459377.5 (2021 July 12).

2. V1674 HER

Seiji Ueda of Japan discovered V1674 Her at $t_{\text{ref}} + 0.5411$ d and promptly posted the discovery to the Central Bureau for Astronomical Telegrams² (CBET 4976). The transient coincides with Gaia DR3 4514092717838547584 at $\alpha = 18:57:30.98324$, $\delta = +16:53:39.5895$, which has a pre-outburst Gaia magnitude of $G = 19.950 \pm 0.020$. The coordinates also match a PanSTARRS source with $g_{\text{ps}} = 20.476 \pm 0.071$, $i_{\text{ps}} = 19.483 \pm 0.024$, and $z_{\text{ps}} = 19.287 \pm 0.004$. Photometry in the PanSTARRS r_{ps} and y_{ps} bands is not given in the DR2 release; however, the source is clearly detected in stacked images in these bands as well.

V1674 Her was also detected by the ZTF survey prior to outburst. We use the ZTF forced-photometry service Masci et al. (2023) to extract the historical g_{ztf} (Fig. 1) and r_{ztf} band photometry. In 2019, the average brightness was $g_{\text{ztf}} = 20.27$, $r_{\text{ztf}} = 18.81$, but the progenitor was brighter and bluer the following year at $g_{\text{ztf}} = 19.74$, $r_{\text{ztf}} = 18.59$, and it remained at this higher level until the 2021 nova eruption. The ZTF observations also reveal significant scatter ($\sigma_g = 0.21$ mag, $\sigma_r = 0.10$ mag), indicating the progenitor is variable on shorter timescales. Periodicity in these variations reveals the spin period of the white dwarf star prior to eruption, $P_{\text{wd}} = 501.4277 \pm 0.0004$ s (Mroz et al. 2021; Drake et al. 2021). At $g_{\text{ztf}} = 19.17$, the ZTF observation on $t_{\text{ref}} - 1.5746$ d is significantly brighter than expected from this trend, and may suggest either flickering or a more steady increase in brightness leading up to the nova outburst (see Fig. 2).

The progenitor system is classified as an intermediate polar in which the white dwarf’s strong magnetic field disrupts the inner accretion disk and funnels the

accreting matter onto the polar regions (Patterson 1994; Patterson et al. 2022). A hot spot forms on the white dwarf’s surface as material accretes, and the intense radiation from this spot modulates as the white dwarf rotates, which results in the observed, short period oscillations in the optical (Mroz et al. 2021).

Around two weeks after discovery a second periodic signal, $P_{\text{orb}} = 0.152934 \pm 0.000034$ d, associated with the orbital period of the binary was also detected in the optical light curve (Schmidt et al. 2021; Shugarov & Afonina 2021; Patterson et al. 2022). The orbital period is typical of novae (Schaefer 2022a), and the implied binary separation ($\sim 1 R_{\odot}$) necessitates a dwarf companion. Using the relation in Knigge (2006) the orbital period implies a companion mass of $0.26 M_{\odot}$.

Optical spectra of V1674 Her were first obtained at $t_{\text{ref}} + 0.84$ d (Munari et al. 2021), which is roughly coincident with maximum light in the visual, and $t_{\text{ref}} + 0.97$ d (Aydi et al. 2021). These first spectra were reported to show broad P-Cygni absorption troughs with minima blue shifted by ~ 3000 km s⁻¹ (see also Habtie et al. 2024). By $t_{\text{ref}} + 1.84$ d the breadth of the lines is reported to have increased to ~ 5000 km s⁻¹. The early spectra are consistent with the Fe II class but with atypically broad lines (Woodward et al. 2021b). Later spectra indicate that V1674 Her entered the nebular phase by $t_{\text{ref}} + 18.4$ d at which point it began to exhibit strong neon lines (Wagner et al. 2021). This implies a ONE WD, and thus an initial WD mass, $M_{\text{WD}} \gtrsim 1.06 M_{\odot}$ (Doherty et al. 2015; Drake et al. 2021).

The distance to V1674 Her is not well constrained. Schaefer (2022b) determine a distance range of 2.5 kpc to 5.4 kpc (68% confidence) using a Bayesian calculation that includes a distance likelihood based on the Gaia DR3 parallax (which peaks at negative values for V1674 Her) and priors based on distributions of nova distances determined through other methods. Sokolovsky et al. (2023) favor a larger distance of 6.3 kpc based in part on a lower limit implied by the optical extinction and 3D dust maps. Considering the observed period and absolute Gaia G magnitude (M_G) distribution of intermediate polars presented in Mukai & Pretorius (2023) (their Fig. 1), we would expect M_G in the 4.2 mag to 6.2 mag range. Given the observed Gaia magnitude in quiescence, this corresponds to a distance range of 2.6 kpc to 6.5 kpc assuming 1.7 mag of absorption in the Gaia band.

Fermi LAT detected 0.1–100 GeV emission coincident with the location of V1674 Her beginning prior to the optical peak (Sokolovsky et al. 2023). The γ -ray source was not present prior to the optical outburst and it faded away in about 18 h.

² <http://www.cbat.eps.harvard.edu/unconf/followups/J18573095+1653396.html>

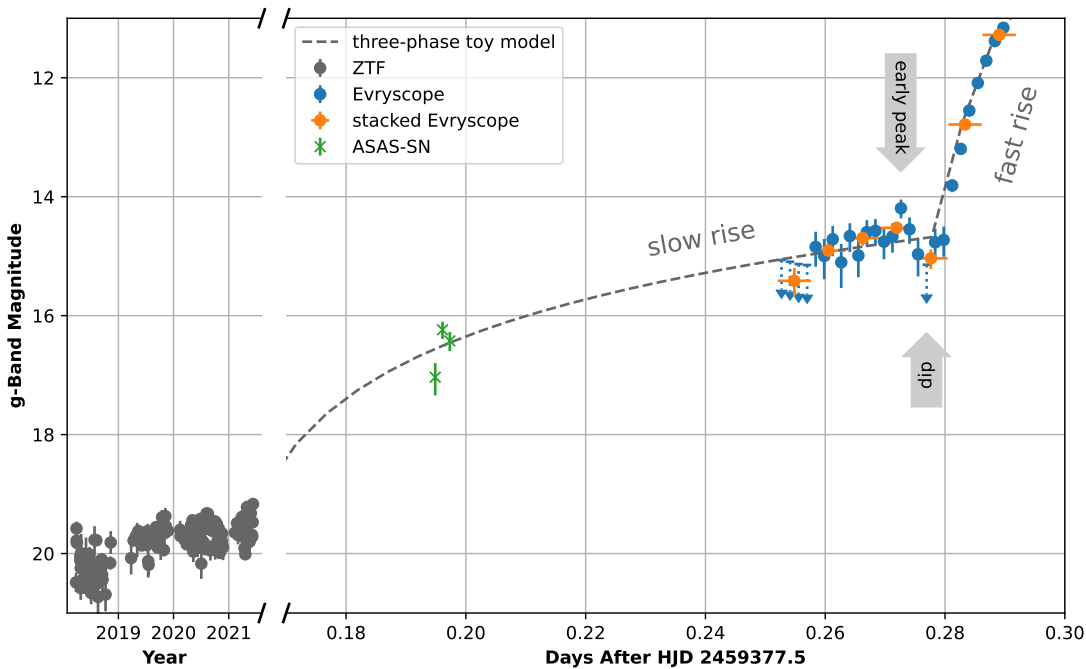


Figure 1. Historical ZTF g -band light curve (grey dots) compared to the earliest ASAS-SN (green Xs) and Evryscope (blue dots) detections. The orange dots are the magnitudes after stacking 4 consecutive Evryscope observations. The dashed line shows the best-fit three-phase toy model (see §5.4). The plot is truncated well below V1674 Her’s visual peak of 6.2 mag at about HJD 2459377.5 +0.84 days to emphasize the early evolution.

Based on K I7699 absorption, [Munari et al. \(2021\)](#) estimate a reddening of $E(B - V) = 0.55$ mag. [Woodward et al. \(2021a\)](#) find a consistent reddening value using the diffuse interstellar band at 6613 Å. Assuming $R_V = 3.1$, this translates into a V -band absorption of $A_V = 1.7$ mag, and for all g -band observations discussed in this paper we assume $A_g = 1.9$ mag.

2.1. Estimates of Key Physical Parameters

Based on the observational constraints (e.g., [Drake et al. 2021](#); [Patterson et al. 2022](#)), we assign a uniform probability for the WD mass in the range $1.0M_\odot \leq M_{\text{WD}} \leq 1.35M_\odot$, and we represent the uncertainty in the companion mass with a Gaussian distribution centered at $M_2 = 0.26 \pm 0.05 M_\odot$. The mass ratio, $q \equiv M_2/M_{\text{WD}}$ is then $q = 0.22 \pm 0.05$, where the uncertainty covers the 68% confidence interval. Following [Eggleton \(1983\)](#) we estimate a volume equivalent radius for the WD’s Roche lobe of $R_{\text{Roche}} \sim (4.8 \pm 0.2) \times 10^{10}$ cm. As the WD expands it may enter a Roche lobe overflow (RLOF) phase where material will flow through the L1 point at $R_{\text{L1}} = (3.0 \pm 0.3) \times 10^{10}$ cm (measured from the center of the WD) and out of the L2 point opposite the companion star at $R_{\text{L2}} = (1.90 \pm 0.07) \times 10^{11}$ cm ([Lu et al. 2023](#); [Shen & Quataert 2022](#)).

The outer radius of the accretion disk, R_{out} , is determined by the circularization radius of matter flowing through the inner Lagrange point (e.g., [Frank et al. 2002](#); their Eq. 4.21),

$$R_{\text{out}} \simeq 4P_{\text{d}}^{2/3}(1+q)^{4/3}[0.5 - 0.23 \log q]^4 R_\odot \quad (1)$$

where $P_{\text{d}} = (P_{\text{orb}}/1 \text{ day})$. For our adopted WD and companion mass uncertainties this results in $R_{\text{out}} = (1.9 \pm 0.1) \times 10^{10}$ cm.

The inner edge of the disk is determined by the Alfvén radius, interior to which the ram pressure of the inflowing gas equals the pressure of the WD magnetic field (e.g., [Frank et al. 2002](#); their Eq. 6.18). We have

$$R_{\text{in}} \simeq 1.4 \times 10^9 \text{ cm} \left(\frac{M_{\text{WD}}}{M_\odot} \right)^{-\frac{1}{7}} \left(\frac{\dot{M}}{10^{-9} M_\odot \text{ yr}^{-1}} \right)^{-\frac{2}{7}} \left(\frac{B_\star}{100 \text{ kG}} \right)^{\frac{4}{7}}, \quad (2)$$

where we take $R_{\text{WD}} \approx 5.4 \times 10^8$ cm for the WD radius and normalize to an accretion rate \dot{M} characteristic of CVs ([Patterson 1984](#)). Depending on the values of \dot{M} and $B_\star \sim 10^5 - 10^7$ G (in the range of intermediate polars), we typically have $R_{\text{out}}/R_{\text{in}} \sim 1 - 10$.

3. OUTBURST PHOTOMETRY

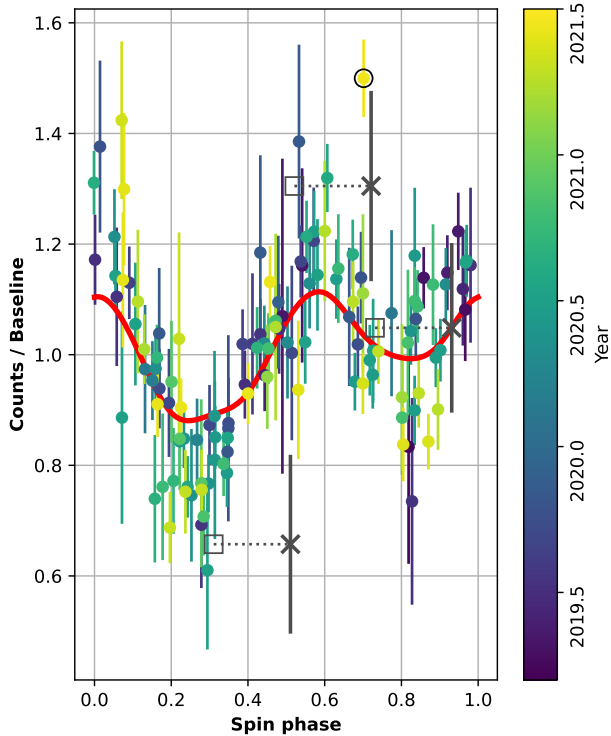


Figure 2. Ratio of the ZTF g -band flux to a best-fit 4th order polynomial fit from 2019 through t_{ref} folded by the 501 s spin period (colored dots). The final, anomalously bright measurement prior to t_{ref} is circled. The red curve shows a spline fit to the better-sampled but lower-amplitude ZTF r -band light curve for comparison. The grey crosses show the first three ASAS-SN detections divided by the best-fit three-phase toy model from §5.4, and the grey squares mark these same values shifted by $0.2P_{\text{wd}}$.

3.1. ASAS-SN Pre-Discovery Detections

The All-Sky Automated Survey for Supernovae (ASAS-SN; Shappee et al. 2014; Kochanek et al. 2017) detected the brightening of V1674 Her prior to its discovery. We use the online ASAS-SN light curve generation interface³ to extract aperture photometry (Table 1). The **bq** camera, which is located at Cerro Tololo International Observatory (CTIO), obtained three consecutive 90 s exposures of the field containing V1674 Her on June 12. The first exposure at $t_{\text{ref}} + 0.1944$ d provides a 4σ detection, and the following two exposures provide $\sim 7\sigma$ detections. None of the prior 425 observations with the **bq** camera that have $\text{FWHM} < 1.9$ pixels (15 arcsec) yield a detection at the 4σ level or higher. To test if neighboring sources contribute significantly to the aperture fluxes we compute the weighted average flux of

³ <https://asas-sn.osu.edu>

these 425 images and find that it is consistent with zero (0.000 ± 0.007 mJy). There are several stars within 15 arcseconds of V1674 Her that should contribute significantly to the aperture sum; however, the field is crowded and it is likely that the sky sample used to estimate the background level contains a similar distribution of field stars. Thus we conclude that the ASAS-SN flux measurements are representative of V1674 Her alone and any light from neighboring sources has been removed through normal background subtraction.

The ASAS-SN light curve generator has an option to measure the flux in stacked images after image subtraction by a reference template. With image subtraction a magnitude of $g = 17.111 \pm 0.136$ is found, but following a similar analysis as above we also find the prior stacked epochs yield a significantly negative average flux of -0.289 ± 0.006 mJy. Thus we believe the image subtraction code is over subtracting the local background and we favor the simple, aperture photometry results on the individual images.

3.2. Evryscope Observations

The early-phase, quick-extraction light curve of V1674 Her as recorded by Evryscope North at the Mount Laguna Observatory has previously been reported (Quimby et al. 2021; Sokolovsky et al. 2023). These data were extracted using aperture photometry and they exclude epochs where any single pixel reached the saturation limit. Here we reanalyze these images to greatly improve the photometry using point spread function (PSF) techniques.

Evryscope North is a system of 20 wide-angle cameras delivering a total field covering 7409 square degrees with 13.1 arcsec pixels down to around 16th magnitude in the g -band every two minutes (Law et al. 2014). Images are processed to remove bias, corrected for flat-field variations, and astrometric solutions are determined using a custom built reduction package (Corbett et al. 2023).

Evryscope North began observing the field of V1674 Her as it rose above airmass 1.5 starting at $t_{\text{ref}} + 0.252$ d. This was 11.4 hours before it reached maximum optical brightness and 7.2 hours before the discovery images were recorded by Seiji Ueda of Japan (CBET 4976). Evryscope North recorded a sequence of sixty exposures, each 2 minutes in duration with ~ 4 s between exposures for readout. Normally the system would rotate to a new sky position at the end of each two hour exposure block and then begin new observations with most fields being imaged by different cameras in the system. However, due to an unknown error the system paused for 50 minutes after the first exposure block before resuming regular operations. In total, three separate cameras recorded

the rise of V1674 Her on the first night of outburst, and four cameras total observed the field on the days before and after the nova outburst.

V1674 Her is located in a crowded field ($b \sim 6^\circ$), and it first appeared in a section of the Evryscope field where the PSF is complex, extended, under-sampled, and highly spatially variable (see Fig. 3). To extract accurate photometry from these data, we have developed new methods to model the PSF and to remove light from contaminating sources. A full description of this procedure is planned for a future paper. In § 3.2.1 and § 3.2.2 we briefly describe the method and present testing to verify the accuracy of the photometry we extract for V1674 Her.

3.2.1. Image Model Subtraction

In classic image subtraction, a reference image (REF) is spatially aligned with a new science frame (NEW) and then convolved with a kernel so that the resulting, convolved REF has the same effective PSF as the NEW. The aligned, convolved REF can then be subtracted from the NEW to produce a residual frame, SUB, that ideally conveys how objects have brightened or faded between the REF and NEW epochs. In reality, SUB frames are typically pocked by errors in the alignment and convolution process that greatly outnumber real astrophysical changes on the sky. These defects are at their worst when the PSF is undersampled and spatially variable, as is the case for the Evryscope North data.

To address this, we separate the PSF into a component that varies with position, P_{xy} , and a component that changes with each exposure, P_t . The effective PSF including the pixel response, P_{xyt} , is the convolution of these two,

$$P_{xyt} = P_{xy} * P_t \quad (3)$$

For Evryscope, the coarse ($13.1''$) pixel scale means that P_t is not significantly dependent on atmospheric seeing and is dominated by small tracking errors. We fit iteratively for P_{xy} and P_t by dividing the CCD into small cells over which we assume P_{xy} is constant and then finding the single P_t for each exposure that best transforms the P_{xy} in each cell to match the data in each cell. With this approach we can assume the PSF to be constant over a much smaller area than would be needed to obtain a set of stars with sub-pixel dither. We only need one star per cell, as we have hundreds of images of each cell. Evryscope tracks the sky for 2 hour blocks, and small tracking errors due to imperfect polar alignment ensure that stars will be dithered as required to properly sample P_{xy} , and we employ enough cells to properly sample P_t on each image.

After we have modeled P_{xyt} over the field, we use an external photometric catalog, ATLAS Refcat2 (Tonry et al. 2018), to set the locations and relative fluxes of sources within each Evryscope field, and then, using the P_{xyt} model, generate a model reference image which can be used to remove quiescent light from the Evryscope images. We refer to this process as, “image model subtraction”. Examples of this technique are shown in Figure 3. The limiting magnitude of Refcat2 ($g \lesssim 19$) is significantly deeper than the Evryscope images ($g \lesssim 16$), which ensures that even sources with marginal flux contributions are included in the reference model. Extended sources are not included in the reference model; however, no such sources are noted in the vicinity of V1674 Her. There are slight effective filter differences between the Evryscope g -band and the Refcat2 g -band which are factored into the model by assuming:

$$g_{\text{evr}} = g_{\text{ps}} + C_1 X + C_2 (g_{\text{ps}} - r_{\text{ps}}) \quad (4)$$

where g_{evr} is the Evryscope g -band magnitude, g_{ps} and r_{ps} are the g and r band magnitudes from Refcat2, respectively, X is the airmass, and C_1 and C_2 are constants determined from a least-squares fit.

3.2.2. Photometry

We produce PSF-fit photometry by scaling P_{xyt} to best match the target flux on each residual image in the least-squares sense (the target is excluded from the image model, so the measured flux represents the actual flux of the target and not the difference from some other epoch). The uncertainty in this scaling is used to set the flux uncertainty. The resulting flux measurements and g -band magnitudes in the ATLAS Refcat2 system (Tonry et al. 2018) are provided in Table 2. We exclude bad or saturated pixels from the PSF fitting, which may increase the systematic uncertainty especially for $g < 10$ mag stars (Table 2 includes only statistical uncertainties). Note that Evryscope has anti-blooming detectors, so when a pixel saturates it does not affect its neighbors.

The photometry originally presented in Quimby et al. 2021 and Sokolovsky et al. (2023) bears some qualitative resemblance to our revised analysis, but there are important differences. First, the initial ~ 40 minutes of observations is now better seen as a slow rise instead of the plateau first reported. The magnitude of these observations are also significantly (~ 1 mag) fainter than previously reported. Evidence for a dip in brightness before the main outburst remains, and a clear peak is now detected prior to this dip. These differences are likely due in part to contaminating sources on the original, aperture photometry pipeline.

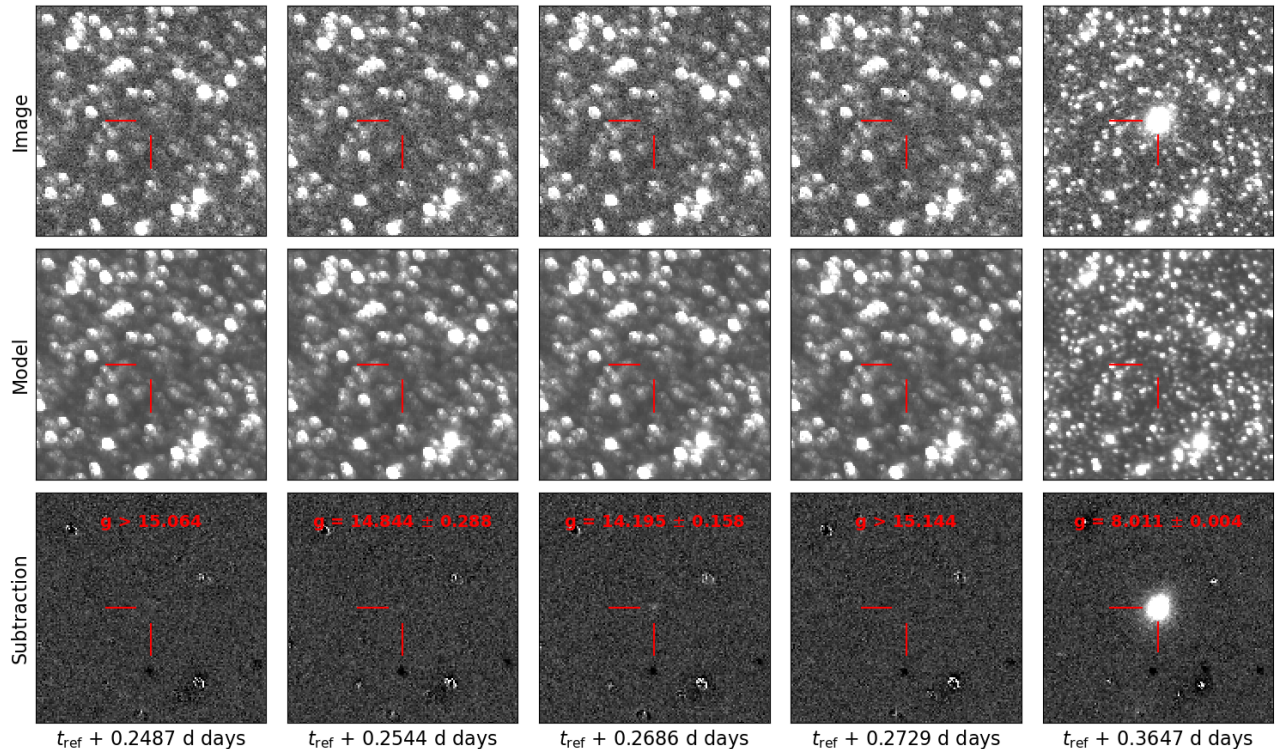


Figure 3. Images centered on V1674 (top row), reference image model (middle row), and corresponding subtractions (bottom row) for select Evryscope observations on June 12th (UT). From left to right: first Evryscope limit ($t_{\text{EVR},0}$); first Evryscope detection ($t_{\text{EVR},0} + 8.2$ min.); early peak ($t_{\text{EVR},0} + 28.7$ min.); the dip ($t_{\text{EVR},0} + 34.9$ min.); first image after the Evryscope ratchet ($t_{\text{EVR},0} + 167.1$ min.). Each image is $30' \times 30'$ and has North up and East left. The red cross hairs mark the position of the nova.

An advantage of image model subtraction is that we have complete control over which sources are included on the reference model and which are not. Thus to validate our photometry we can select any star in the field, exclude it from the reference model, and then measure the residual brightness on the subtracted image. We perform this procedure for a few thousand stars in the field and then use the measured residuals to determine the 50% completeness limit for each image. These limits are provided along with the photometry in Table 2. Additionally, we produce light curves for these field stars and use them to check the error estimates by comparing the average error to the standard deviation of the light curve over a broad range of mean source brightness. We find that the error bars for $g > 14$ mag stars are typically overestimated by about 30%. By $g \sim 12$ mag the measured uncertainties are well matched to the measured light curve standard deviations, and brighter stars have underestimated uncertainties.

4. LIGHT CURVE ANALYSIS

The rising portion of the V1674 Her outburst captured on June 12th by ASAS-SN and Evryscope can be divided into at least three parts: 1) an initial ~ 5 mag brighten-

ing compared to the quiescent ZTF measurements in 2021; 2) a subsequent, one hour period over which the flux increases by a factor of ~ 11.5 in a roughly linear fashion; and 3) the next 3.5 hours over which the flux continues to increase linearly with time but at a higher rate. We refer to these phases, respectively, as the “slow rise,” “fast rise”, and “faster rise,” and discuss each of these in the following sections.

4.1. Slow Rise

The first pre-discovery detections by ASAS-SN and Evryscope demonstrate a flux increase of about 5.5 times over 1.8 hours. The first ASAS-SN measurement is significantly fainter than the second, which indicates variability on minute timescales. The 105 s spacing between the first and second ASASS-SN observations corresponds to roughly 1/5 of the spin period measured by ZTF. If the spin period is constant from the pre-outburst ZTF measurements, the midpoints of these two exposures should not represent extreme phases of the prior spin variability (see Fig. 2). However, the relative variability in the ASAS-SN photometry is quite similar to the historical ZTF trend if we arbitrarily shift the phase of the ASAS-SN measurements by 1/5 of the spin period.

Thus, it is possible that the variations in the ASAS-SN light curve are related to the spin of the WD with a difference in phase compared to the ZTF light curve.

The first four Evryscope North observations yield low-significance detections (formally $\sim 2.3\sigma$, but correcting for the over-estimated uncertainty noted in §3 the significance would be above 3σ), and the target is seen to brighten significantly at an average rate of 0.108 ± 0.021 mJy min $^{-1}$ through the 14th measurement. The following observation with a mid-exposure time of $t_{\text{ref}} + 0.2726$ d is roughly 2σ brighter than this trend and is followed by a fading at a rate of 1.030 ± 0.052 mJy min $^{-1}$ over the next 6.1 minutes, which culminates in the lowest significance detection (formally $\sim 1.1\sigma$) at $t_{\text{ref}} + 0.2769$ d. We refer to this epoch as the “dip” and to the prior maximum as the “early peak” (Fig. 1).

Prior to the early peak the flux increase shown by Evryscope is consistent with a linear rise. However, extrapolating this trend back in time would predict negative flux at the ASAS-SN epochs. A joint fit to the ASAS-SN and first 14 Evryscope measurements results in an assumed linear brightening rate of 0.0324 ± 0.0015 mJy min $^{-1}$, which is significantly slower than the rate derived from the first 14 Evryscope points alone. If we assume the initial flux increase can be fit with a power law:

$$f(t) \propto (t - t')^n \quad (5)$$

we find that larger values of n are preferred, but do not significantly improve the match to the steeper Evryscope rise as compared to $n = 1$.

4.2. Fast Rise

After the dip a dramatic brightening phase begins at $t_{\text{ref}} + 0.2812$ d with a flux increase factor of 2.3 ± 0.6 over the previous Evryscope exposure. The brightening rate rapidly approaches an average of 13.80 ± 0.07 mJy min $^{-1}$ and remains nearly constant for about 1 hour. Over this period the flux increases by a factor of 185 with typical deviations from the linear model of only 1%. We fit Equation 5 to these data and find a best-fit power-law index of $n = 1.07 \pm 0.01$ (and $t' = t_{\text{ref}} + 0.2824 \pm 0.0002$ d), which indicates a nearly linear rise is favored. For comparison, the initial brightening rate of T Pyx, which is known for its rapid initial rise (Schaefer et al. 2013), averages to just ~ 1.0 mJy min $^{-1}$ for a factor of 2 increase over a 1.8 hour period.

4.3. Faster Rise

The first two-hour observing block ends with 4 measurements that deviate slightly from the fast rise trend. When the next camera began observing again after the

50 min technical delay the measured fluxes are $\sim 30\%$ brighter than predicted by the fast rise trend. This indicates a break in the light curve to a higher rate of flux increase occurs near the end of the first observing block. The rate of brightening is about 63% higher compared to the fast rise phase. Fitting only measurements between $0.3282 \text{ d} < t - t_{\text{ref}} < 0.4591 \text{ d}$ we find a best-fit power-law index of 0.97 ± 0.02 (and $t' = t_{\text{ref}} + 0.3020$ d), which is again consistent with a linear rise, this time at a rate of 22.46 ± 0.11 mJy min $^{-1}$. We cannot rule out a small (~ 0.05 mag level) systematic offset between the first and second camera measurements, but such a shift would have minimal impact on the linearity of the rise. We also note that a third Evryscope camera began observing the field of V1674 Her starting at $t_{\text{ref}} + 0.4535$ d. We truncate the data from this camera at 18 degree morning twilight, but the 5 observations prior to twilight appear consistent with the same linear trend.

Extrapolating this linear rise, we would expect V1674 Her to be near $g = 6.7$ mag at the time of discovery ($t_{\text{ref}} + 0.5411$ d); however, the reported discovery magnitudes are 8.4 and 8.0 on the discoverer’s Canon EOS 6D digital camera. We find it likely that the nova is saturated on the discovery images because shortly after they were taken, the nova was confirmed by Koichi Itagaki at a CCD magnitude of 6.7 at $t_{\text{ref}} + 0.5551$ d. This is about 0.1 mag fainter than a continuation of the linear brightening observed by Evryscope predicts, which is likely within systematic uncertainties. Thus, V1674 Her may have continued rising roughly linearly in the optical through Mr. Itagaki’s confirmation image.

5. NOVA MODELS

In this section we discuss models that could potentially explain features of the rising light curve. We consider heating of the WD photosphere by thermonuclear fusion in §5.1. In §5.2 we develop a toy model based on expansion of the WD envelope at constant luminosity and use it to place physical constraints on the outburst. In §5.3 we consider how X-rays emitted from the hot WD envelope may be reprocessed into optical light by the accretion disk or companion, and we introduce a three-phase toy model in §5.4 with constant velocities in each phase to represent slow, fast, and faster expansion of the WD envelope.

5.1. Thermonuclear Heating

In the classic picture of a nova, when the convective envelope reaches the WD’s photosphere its temperature begins to increase but at first the radius remains roughly constant (e.g., Prialnik et al. 1979). The WD only begins to expand when the bolometric luminosity reaches the Eddington limit, which is about

$1.4 \times 10^{38} \text{ erg s}^{-1}$ for a solar mass WD. Assuming a WD radius of $R_0 = 5400 \text{ km}$, this luminosity is reached when the effective surface temperature reaches a peak of about $T_{\text{max}} = 9 \times 10^5 \text{ K}$. Thus before expansion sets in the absolute g -band magnitude of the WD would be about $M_g \sim 6.3$. For the distance and line-of-sight absorption appropriate to V1674 Her ($D \gtrsim 3 \text{ kpc}$; $A_g = 1.9 \text{ mag}$), the predicted brightness at T_{max} is $g \gtrsim 20.6 \text{ mag}$. This limit is comparable to observations of the system in quiescence and, critically, much too faint to explain the early ASAS-SN and Evryscope observations. We next consider if the early detections are consistent with expansion of the WD.

5.2. Toy Model: Expansion at Constant Luminosity

As thermonuclear fusion drives the luminosity of the nova to the Eddington limit the WD begins to expand, but the bolometric luminosity settles at a roughly constant value (e.g., Gallagher & Code 1974). Thus the WD surface temperature cools from T_{max} , and the peak of the SED moves from the X-ray to the UV and finally into the optical. We now construct a toy model to represent this process and compare it to the observations.

For a blackbody expanding at constant luminosity the temperature, T , will decrease as the radius, R increases following

$$T = T_{\text{max}} \left(\frac{R_0}{R} \right)^{1/2} \quad (6)$$

Assuming the expansion velocity quickly reaches a steady velocity, v , we can write

$$R = R_0 + v(t - t'_0), \quad (7)$$

for $t > t'_0$, where t'_0 is the time at which the expansion begins. The toy model then predicts an observed flux density given by

$$f_\nu = \pi B_{\nu,T} \left(\frac{R}{D} \right)^2, \quad (8)$$

where $B_{\nu,T}$ is the Planck function for temperature T . For any given time we can then set the radius and temperature using equations 6 and 7, compute f_ν , and then convolve this spectral energy distribution with an optical band pass to recover the classic light curve of a nova outburst characterized by a smooth rise to peak followed by a slower decline.

However, this toy model cannot even qualitatively explain the distinct sections recorded in the rise of V1674 Her. The toy model lacks the initial, slow rise and transition into a fast rise exhibited by V1674 Her, and it further lacks the second transition to a faster rise before the peak. The slow decline of the toy model relative to

its fast rise also does not appear to match the rather symmetric rise and decline of V1674 Her around peak (see Fig. 4).

We next consider the brightness predicted by the toy model at key stages of the nova's development. The observed flux may exceed these predictions if other sources of power are present, but we can use the toy model to rule out some situations where the observed fluxes fall below the toy model predictions.

We begin by considering the expected brightness of the WD as it expands to fill its Roche lobe. With the bolometric luminosity fixed at the Eddington limit and approximating the emitting surface using the volume equivalent radius (Eggleton 1983), the g -band magnitude would be between about 14.9 mag and 13.4 mag for distances of 6 kpc to 3 kpc, respectively, assuming $A_g = 1.9$. Thus at the higher distance the predicted flux roughly corresponds to the brightness first reached near the early peak. To put it another way, the WD was unlikely to have filled its Roche lobe prior to the early peak.

Another important radius to consider is the outer radius of the accretion disk, $R_{\text{out}} \approx 1.9 \times 10^{10} \text{ cm}$, (see §2.1). Again considering distances of 3 kpc to 6 kpc, the toy model predicts $14.9 \text{ mag} < g < 16.4 \text{ mag}$. Thus, the observed slow rise to peak could be consistent with the WD expanding to R_{out} if the distance to the nova is at the low end. In this case, the implied expansion velocity averaged just 20 km s^{-1} over the 2.3 hours before the fast rise. This is orders of magnitude slower than the escape speed from a $\sim 1.0 M_\odot$ WD at a radius of R_{out} .

When the temperature cools to roughly $1.5 \times 10^5 \text{ K}$, the opacity increases due to the presence of iron-peak elements, and this is expected to launch a fast, line-driven wind (Kato & Hachisu 1994). With our assumed R_0 and T_{max} , the toy model predicts that this temperature is reached at roughly R_{out} . Thus it is plausible that the fast rise following the initial slow rise in the Evryscope light curve represents the launch of the fast wind.

5.3. Reprocessing by Accretion Disk and Secondary

Another important process to consider at the earliest phases of the nova outburst is the reprocessing of X-rays emitted by the hot WD in the accretion disk or irradiated side of the companion. We start by considering reprocessing by the accretion disk. At a given distance r from the WD, a fraction $\sim H/R_{\text{out}}$ of the total solid angle is subtended by the accretion disk, where H is the vertical scale-height of the disk and the aspect ratio H/r is calculated near the outermost radius of the disk $r \approx R_{\text{out}}$ because H/r typically increases with r . The

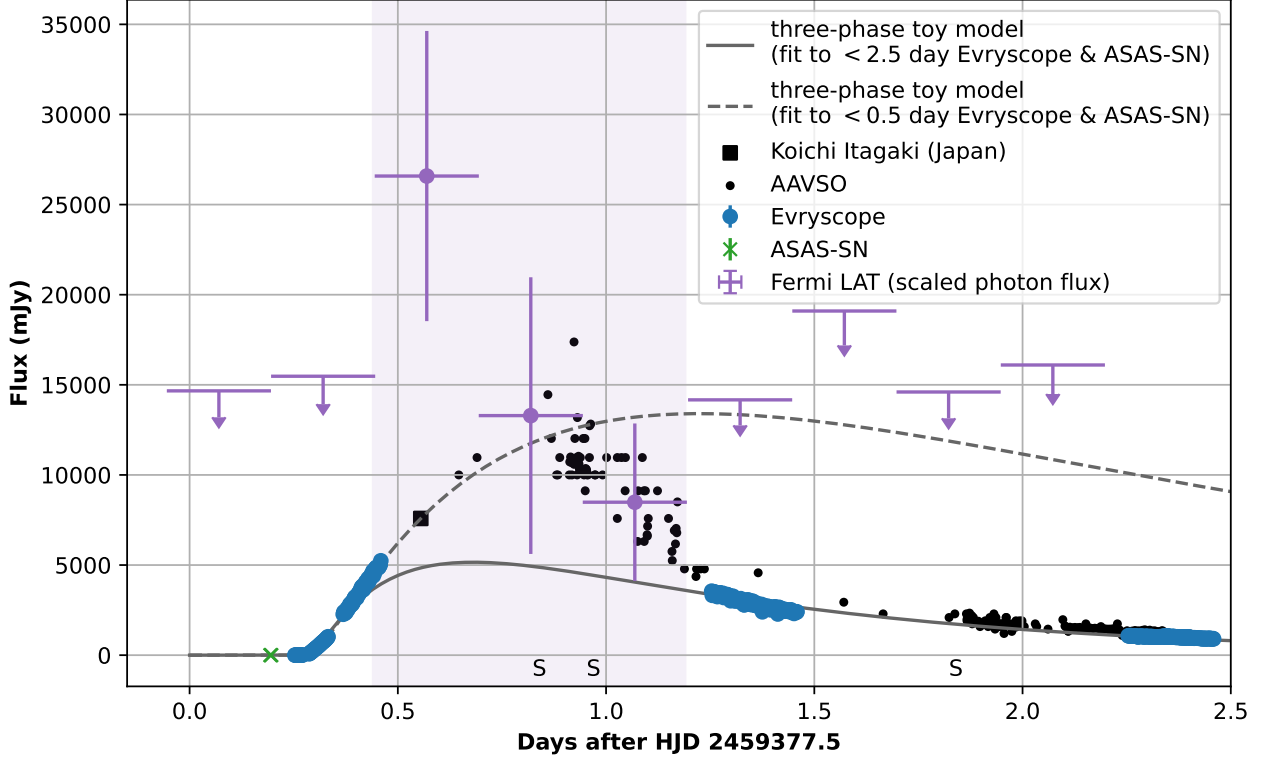


Figure 4. Three-phase toy model fits (grey curves) to the ASAS-SN and Evryscope measurements. Black points are AAVSO measurements (Kloppenborg, B. K. 2023), either visual or in the V-band, which are plotted as equivalent to g -band fluxes assuming no systematic offsets and are not included in the fitting. Purple dots give the Fermi/LAT photon flux from Sokolovsky et al. (2023) arbitrarily scaled to align the last two detections with the AAVSO measurements. The time span covering the Fermi/LAT detections is highlighted, and limits are shown outside this range with down pointing arrows. The first reported epochs of optical spectroscopy are marked with “S” (Munari et al. 2021; Aydi et al. 2021).

reprocessed luminosity is therefore given by

$$L_{\text{rep}} \sim (H/R_{\text{out}})L_{\text{WD}}(1 - \mathcal{A}), \quad (9)$$

where \mathcal{A} is the albedo of the disk surface, which we expect to be of order unity because of the significant neutral fraction of the disk material (e.g., van Paradijs 1983). Prior to the nova outburst, we expect $H/r \sim 0.03$ on radial scales $r \sim R_{\text{out}}$, depending weakly on the disk viscosity parameter α and \dot{M} (e.g., Frank et al. 2002; their Eq. 5.49). However, H/r may be somewhat larger than this estimate as a result of irradiation heating dominating over internal viscous heating of the disk.

Equating the flux of radiation $F_{\text{heat}} \simeq L_{\text{rep}}/(2\pi r^2)$ to the rate of radiative cooling $F_{\text{cool}} \simeq 2\pi\sigma T_{\text{rep}}^4$, gives an estimate of the effective temperature for the reprocessed disk emission,

$$T_{\text{rep}} \simeq \left(\frac{(H/r)L_{\text{WD}}(1 - \mathcal{A})}{4\pi^2\sigma r^2} \right)^{1/4} \approx 3.9 \times 10^4 \text{ K} \times \left(\frac{R_{\text{out}}}{2 \times 10^{10} \text{ cm}} \right)^{-1/2} \left(\frac{L_{\text{WD}}}{1.4 \times 10^{38} \text{ erg s}^{-1}} \right)^{1/4} \times$$

$$\left(\frac{H/r}{0.03} \right)^{1/4}, \quad (10)$$

where we have taken $\mathcal{A} = 0.5$ (e.g., van Paradijs 1983) and normalize r to R_{out} from Eq. 1.

Blackbody emission of temperature $T_{\text{rep}} \approx 4 \times 10^4 \text{ K}$ peaks above the optical g -band $\nu_{\text{opt}} \approx 6 \times 10^{14} \text{ Hz}$ of our observations. If both the WD and the reprocessed emission are observed in an optical band on the Rayleigh-Jeans tail of a blackbody (i.e., $h\nu \ll kT_{\text{rep}}, kT_{\text{WD}}$), the ratio of their optical band luminosities can be written,

$$\frac{L_{\text{opt,rep}}}{L_{\text{opt,WD}}} \approx \frac{R_{\text{out}}^2 T_{\text{rep}}}{R_{\text{WD}}^2 T_{\text{WD}}} \approx 13.5 \left(\frac{H/r}{0.03} \right)^{1/4} \left(\frac{R_{\text{WD}}}{0.03 R_{\text{out}}} \right)^{-3/2} \quad (11)$$

The reprocessed luminosity can thus dominate the optical light curve, until the white dwarf has begun to expand significantly from its initial radius ($R_{\text{WD}} \gtrsim 0.2R_{\text{out}}$). After this point, the white dwarf photosphere will soon come to dominate and the light curve will begin to rise faster. This scenario could possibly be at play in the slow-rise phase with the ASAS-SN measurements dominated by reprocessed light and the Evryscope ob-

servations dominated by the WD photosphere. Alternatively, if the WD engulfs the disk somewhat prior to dominating the optical luminosity this might create a brief dip in the light curve after the disk is destroyed, similar to what is observed.

The companion star can be an equally if not more important source of reprocessing (e.g., van Paradijs & McClintock 1994). In particular, the ratio of the solid angle subtended by the secondary to that subtended by the disk is given by

$$\frac{\Omega_\star}{\Omega_d} \approx \frac{\pi R_2^2 / a_{\text{bin}}}{2\pi R_{\text{out}}(H/r)} \approx 4 \left(\frac{R_2}{0.3R_\odot} \right)^2 \left(\frac{H/r}{0.03} \right)^{-1}, \quad (12)$$

where $R_2 \approx 0.3R_\odot$ is the characteristic radius of CV donors of mass $M_2 \approx 0.3M_\odot$ (e.g., Knigge 2006) and we have taken $a_{\text{bin}} \approx 8 \times 10^{10}$ cm for the binary separation. Reprocessing by the donor star may even dominate that by the accretion disk, depending on H/r . Indeed, periodic modulation of nova light curves due to irradiation of the companion, has been reported for V1974Cyg (De Young & Schmidt 1994), V407Lup (Aydi et al. 2021), V392 Per (Munari et al. 2020; Murphy-Glaylor et al. 2022); however, in most cases this modulation is observed *after* the peak of the outburst, 2-4 mag below the peak brightness (see Schaefer 2022a for a review).

5.4. Three-Phase Toy Model

Motivated by the three distinct parts of the observed rise to peak we next consider a version of the toy model in which the expansion rate has 3 parts. We adopt the same assumptions as before, namely that the nova is a blackbody emitter and that the temperature drops as the radius increases to maintain a constant bolometric luminosity. We maintain the simplification that the photospheric radius increases linearly with time, but here we allow the photospheric velocity in each phase to differ. We can then fit for the times each phase begins and the velocities of the photosphere in each phase, and optionally the distance, initial radius, R_0 , and initial temperature, T_{max} at the start of the expansion phase.

The best-fit three-phase toy model is shown in Figures 1 and 4, and the best-fit radius and temperature evolution is shown in Figure 5. The fit favors a low distance, $D = 2.8$ kpc, but the precise value is uncertain given that distance is degenerate with luminosity (and thus R_0 and T_{max}). It is suggestive, however, that the best-fit temperature curve drops to near the range where the opacity is expected to increase significantly due to iron-peak elements (about 1.5×10^5 K) at roughly the same time that the fast rise begins. The best-fit velocity for the fast rise is about 2000 km s^{-1} , and this increases to about 2800 km s^{-1} in the faster rise phase, which is

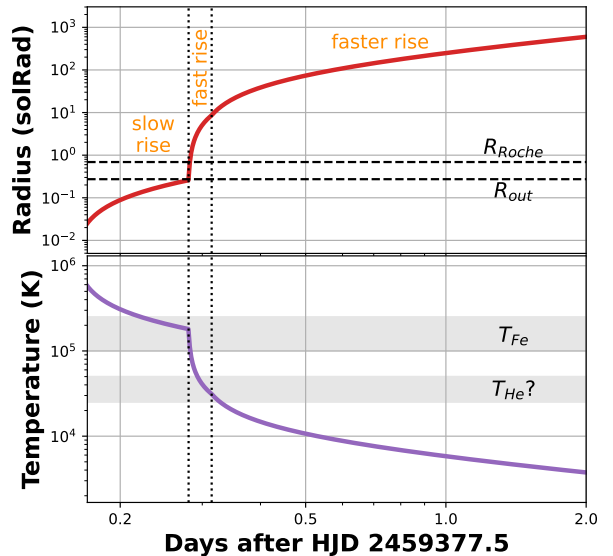


Figure 5. Radius and temperature evolution of the best-fit three-phase toy model. Dashed lines mark the estimated, volume-equivalent Roche lobe radius, R_{Roche} , and the outer disk radius, R_{out} . Approximate temperature ranges where higher opacities are possible (depending on density) are indicated by the light-gray bands.

reminiscent of the 3000 km s^{-1} absorption features observed in the early spectra (Munari et al. 2021; Aydi et al. 2021).

Although the three-phase toy model can account for the slow and fast rise phases and it can account for the observed light curve in the first days following peak, it is not able to fit V1674 Her around the time of optical maximum and it begins to fade faster than the data starting a couple days after peak. Observations of γ -rays and X-rays over these periods have implied the presence of shocks, which may further bolster the optical flux from V1674 Her over the predictions of the three-phase toy model. In Figure 4 we also show a three-phase toy model fit to the earliest, $t < t_{\text{ref}} + 0.5$ d data only. In this case the post-peak brightness is greatly over predicted, and the best-fit distance, 1.3 kpc, is much lower.

6. DISCUSSION AND CONCLUSIONS

The first ASAS-SN detections combined with the high-cadence monitoring of Evryscope provide an unprecedented picture of the optical rise of a fast nova. The departure from quiescence may have begun with the anomalously bright detection of V1674 Her by ZTF on $t_{\text{ref}} - 1.5746$ d, which is 2.4 d before the estimated date of V-band maximum (Appendix A). The following observations by ASAS-SN starting at $t_{\text{ref}} + 0.1944$ d

mark a ~ 3 mag rise in brightness over the ZTF baseline and show variability on timescales consistent with the WD spin period but out of phase. V1674 Her was observed with a 2 min cadence by Evryscope starting at $t_{\text{ref}} + 0.2527$ d when it was already ~ 1 mag brighter than the ASAS-SN average. It reached an early peak minutes later, and then faded significantly before rebounding and then starting a fast, almost linear rise in flux for 1 hour. This was followed by a second break to a faster, even more linear rise through at least the next 3 hours when morning twilight began for Evryscope.

The rough consistency between the initial ASAS-SN detections and the shape of the historical ZTF phase-folded light curve implies that the accretion spot remains a dominant source of power at these early phases of the outburst. If the g -band flux scales linearly with the accretion rate, \dot{M} , then \dot{M} increases by a factor of ~ 15 over the historical ZTF rate. Such a scenario might occur during the X-ray flash as the X-ray luminosity of the WD increases and begins ablating the companion, similar to what [Patterson et al. \(2022\)](#) argue takes place during the soft X-ray phase after optical maximum. Photoevaporation of the disk might also lead to an increase in the aspect ratio of the disk, H/r , which would increase the reprocessed luminosity and perhaps explain the brightening trend from the first ASAS-SN detections to the first Evryscope detections. Alternatively, these ASAS-SN and Evryscope observations are separated by roughly half the orbital period, so the change in brightness might reflect the projected area of the reprocessing region, although some fine-tuning is required in this case to have the peak immediately prior to the start of the fast rise.

Assuming instead that the rise of V1674 Her is powered exclusively by changes in the temperature and radius of the WD photosphere, we can parameterize the slow, fast, and faster rising phases with a three-phase toy model. The model assumes a blackbody radiating constantly at the Eddington luminosity and thus cooling as the photosphere expands slowly at first, then fast, then faster. The best-fit model begins with a gentle expansion characterized by a photospheric velocity, $v_{\text{ph},1}$, of $\sim 20 \text{ km s}^{-1}$, and then transitions to a fast wind, $v_{\text{ph},2} \sim 2000 \text{ km s}^{-1}$. At the transition point, the model favors a photospheric temperature of around $T_{\text{ph}} \sim 1.5 \times 10^5 \text{ K}$, which is in the range where iron-peak elements produce an opacity peak (see Fig. 5). Such an increase in opacity has been discussed as the impetus for an optically thick wind ([Kato & Hachisu 1994](#)). The best-fit toy model has a photospheric radius of $\sim 0.26 R_{\odot}$ at the point where the photospheric velocity increases to $v_{\text{ph},2}$. The escape velocity for a $1.3 M_{\odot}$

WD with this radius is $v_{\text{esc}} \sim 1400 \text{ km s}^{-1}$, so the toy model provides a roughly consistent picture of a WD envelope cooling into the iron opacity bump and launching an optically thick wind.

However, the toy model does not predict a dip in flux just prior to the fast rise as is observed in the Evryscope light curve. If the fast rise represents the launch of an optically thick wind brought on by a sudden increase in opacity, then perhaps this sudden opacity increase also momentarily diminishes the g -band flux? It is not obvious that this will happen because the photospheric radius will increase and the temperature will further decrease as the wind is launched, which will ultimately increase the optical flux. Models implementing radiation hydrodynamics are needed to study this transition in more detail. If the dip is connected to a sudden increase in opacity, then single-band, high-cadence observations like these from Evryscope provide precise times at which the WD photosphere reaches a known temperature and will thus provide powerful modeling constraints. Alternatively, this transition may occur coincidentally to the envelopment of the accretion disk by the expanding WD envelope, which would quickly put an end to any X-ray reprocessing that may have been supplementing the optical flux, resulting in a g -band dip. In this case, observations of other novae may not have a dip immediately prior to the launch of a fast wind.

The third, faster rising portion of the early V1674 Her light curve is also difficult to explain in the context of the three-phase toy model. Fitting to only the ASAS-SN and Evryscope data obtained prior to optical maximum, the model can account for the linear rising trends in the Evryscope data and make reasonable predictions for the pre-maximum observations recorded by amateurs; however, it cannot explain the rapid post maximum fading. Physically, we would expect the toy model to break down as the outer envelope thins and the photosphere begins to recede. For comparison, the fastest evolving model considered by [Kato et al. \(2024\)](#), a $1.3 M_{\odot}$ WD with a $2 \times 10^{-6} M_{\odot}$ carbon enriched envelope, takes 2.5 days to reach this point after the shell flash (defined as the moment of maximum nuclear luminosity), whereas the optical peak of V1674 Her occurs just 0.64 days after the first ASAS-SN detection. Thus, if the optical peak corresponds to the time the photosphere is its largest, then the envelope mass is likely significantly smaller than $2 \times 10^{-6} M_{\odot}$. Alternatively, perhaps the final, anomalously bright ZTF measurement prior to outburst (see Fig. 2) better reflects the start of the shell flash. In this case the observed rise to optical maximum, 2.4 d, would be an excellent match to the [Kato et al. \(2024\)](#) model.

If we extend the three-phase toy model fitting to include the first 3 days of Evryscope observations, the best-fit model provides an acceptable fit to the data *except* for the period over which γ -rays were detected by Fermi. This could indicate that the optical peak was powered by the same shocks responsible for the γ -rays. Previous studies have shown correlations between γ -rays and optical light around peak (Li et al. 2017), and Sokolovsky et al. (2023) find that the ratio of γ -ray to optical luminosity extrapolated over the optical peak of V1674 Her, $L_\gamma/L_{\text{opt}} \sim 1/500$, is consistent with other γ -ray novae. Munari et al. (2017) have shown that some light curves can be decomposed into fireball and γ -ray components. V1674 Her may be a similar event. The transition from a fireball dominated light curve to a γ -ray dominated light curve may also explain the pre-maximum halts observed 0.5–2 mag below peak in some (Hounsell et al. 2010) but not all (e.g., Thompson 2017) novae. These halts have alternatively been explained as a momentary dip in flux resulting from the convective zone dropping below the WD’s photosphere as mass-loss begins (Hillman et al. 2014). The Evryscope light curve of V1674 Her rules out such a pre-max halt within 1–8 mag of peak, but the same physical process might explain the early dip even though it is an unprecedented 8.5 mag below peak brightness.

The detection of γ -rays can be understood in connection to the photospheric velocity increase implied by the best-fit three-phase toy model if shocks are produced from interaction of the second, faster wind with the first, slower wind. The velocity of an optically thick wind is typically connected to the escape velocity. As the photosphere expands, this velocity decreases. In the models of Hachisu & Kato (2022), shocks are formed after optical maximum as the photosphere begins to recede and the wind velocity thus increases and begins shocking the prior wind. Thus they predict the γ -rays should begin after optical maximum, but for V1674 Her the first Fermi detection comes prior to optical maximum. However, Quataert et al. (2016) have discussed internal shocks in outflows driven by (locally) super-Eddington winds. In this scenario the initial wind essentially clears a path for the later wind, which can then run through pre-expanded, lower-density material at higher velocities. Shocks are then produced when this late wind interacts with the early wind, which may explain the early γ -ray emission in V1674 Her.

The γ -ray emission from previous novae has been explained in the context of a fast wind interacting with a slow torus of gas that is formed when the WD overflows its Roche lobe and material is ejected by the companion. If this is the case for V1674 Her, then the linear rise in

flux constrains the density profile of the slow torus to be $\rho \propto r^{-3}$, which is close to radial behavior expected close to the WD (Pejcha et al. 2016). In this case the faster wind would need to be launched by $t_{\text{ref}} + 0.314$ d, which is only 1.9 d after the anomalously bright ZTF measurement. However, it is difficult to explain the Evryscope light curve in the context of the fast-wind, slow-torus paradigm because the ASAS-SN and Evryscope observations are fainter than the toy model predicts the WD to be during RLOF until the fast rise begins, and this transition comes only hours before the first Fermi/LAT detection. Thus, there does not appear to be sufficient time for material to stream out of the L2 nozzle and form the slow torus. The spectra of some other novae indicate the presence of such relatively slow moving gas (Aydi et al. 2020a), but the lowest velocity features noted in the earliest spectra of V1674 Her are P-Cygni profiles with absorption troughs blue-shifted by ~ 3000 km s $^{-1}$ (Munari et al. 2021; Aydi et al. 2021). Spectra taken the following days exhibit complex line profiles that favor multiple velocity flows (Woodward et al. 2021a) instead of a single fast wind interacting with a single slow wind. It thus appears that the WD began its rapid expansion prior to extensive stripping by the companion. If RLOF begins with the fast rise and shocks begin with the faster rise, then the companion has only $\sim 22\%$ of an orbit to spray material out the L2 nozzle.

The observational signature marking the start of a nova outburst has long been predicted to take the form of a UV/X-ray flash (Starrfield et al. 1990). However, such data remain scarce due to the limited sensitivity and sky coverage of X-ray instruments (but see König et al. 2022). V1674 Her demonstrates an alternative path to studying the earliest phases of novae using wide-field, high-cadence optical surveys like Evryscope and the planned Argus Array (Law et al. 2022). With a depth of $g < 19.6$ mag at 60 s cadence and a simultaneous ~ 8000 square degree field of view, Argus will be capable of recording the optical brightening during the rise to T_{max} and optical signatures of the X-ray flash of nearby (< 5 kpc) novae.

We acknowledge with thanks the variable star observations from the AAVSO International Database contributed by observers worldwide and used in this research. The ZTF forced-photometry service was funded under the Heising-Simons Foundation grant #12540303 (PI: Graham). B.D.M. acknowledges support from NASA through the Astrophysics Theory Program (grant 80NSSC22K0807) and Fermi Guest Investigator program (grant 80NSSC24K0408). The Flatiron Institute is supported by the Simons Foundation. K.J.S. acknowledges support by NASA through the Astrophysics Theory Program (80NSSC20K0544).

REFERENCES

- Ackermann, M., Ajello, M., Albert, A., et al. 2014, *Science*, 345, 554, doi: [10.1126/science.1253947](https://doi.org/10.1126/science.1253947)
- Aydi, E., Chomiuk, L., Izzo, L., et al. 2020a, *ApJ*, 905, 62, doi: [10.3847/1538-4357/abc3bb](https://doi.org/10.3847/1538-4357/abc3bb)
- Aydi, E., Sokolovsky, K. V., Chomiuk, L., et al. 2020b, *Nature Astronomy*, 4, 776, doi: [10.1038/s41550-020-1070-y](https://doi.org/10.1038/s41550-020-1070-y)
- . 2021, *The Astronomer’s Telegram*, 14710, 1
- Aydi, E., Chomiuk, L., Mikołajewska, J., et al. 2023, *MNRAS*, 524, 1946, doi: [10.1093/mnras/stad1914](https://doi.org/10.1093/mnras/stad1914)
- Bellm, E. C., Kulkarni, S. R., Graham, M. J., et al. 2019, *PASP*, 131, 018002, doi: [10.1088/1538-3873/aaecbe](https://doi.org/10.1088/1538-3873/aaecbe)
- Bhargava, Y., Dewangan, G. C., Anupama, G. C., et al. 2024, *MNRAS*, 528, 28, doi: [10.1093/mnras/stad3870](https://doi.org/10.1093/mnras/stad3870)
- Chomiuk, L., Metzger, B. D., & Shen, K. J. 2021, *ARA&A*, 59, 391, doi: [10.1146/annurev-astro-112420-114502](https://doi.org/10.1146/annurev-astro-112420-114502)
- Chomiuk, L., Linford, J. D., Yang, J., et al. 2014, *Nature*, 514, 339, doi: [10.1038/nature13773](https://doi.org/10.1038/nature13773)
- Corbett, H., Carney, J., Gonzalez, R., et al. 2023, *ApJS*, 265, 63, doi: [10.3847/1538-4365/acbd41](https://doi.org/10.3847/1538-4365/acbd41)
- De Young, J. A., & Schmidt, R. E. 1994, *ApJL*, 431, L47, doi: [10.1086/187469](https://doi.org/10.1086/187469)
- Doherty, C. L., Gil-Pons, P., Siess, L., Lattanzio, J. C., & Lau, H. H. B. 2015, *MNRAS*, 446, 2599, doi: [10.1093/mnras/stu2180](https://doi.org/10.1093/mnras/stu2180)
- Drake, J. J., Ness, J.-U., Page, K. L., et al. 2021, *ApJL*, 922, L42, doi: [10.3847/2041-8213/ac34fd](https://doi.org/10.3847/2041-8213/ac34fd)
- Eggleton, P. P. 1983, *ApJ*, 268, 368, doi: [10.1086/160960](https://doi.org/10.1086/160960)
- Frank, J., King, A., & Raine, D. J. 2002, *Accretion Power in Astrophysics: Third Edition*
- Gallagher, J. S., I., & Code, A. D. 1974, *ApJ*, 189, 303, doi: [10.1086/152804](https://doi.org/10.1086/152804)
- Gallagher, J. S., & Starrfield, S. 1978, *ARA&A*, 16, 171, doi: [10.1146/annurev.aa.16.090178.001131](https://doi.org/10.1146/annurev.aa.16.090178.001131)
- Graham, M. J., Kulkarni, S. R., Bellm, E. C., et al. 2019, *PASP*, 131, 078001, doi: [10.1088/1538-3873/ab006c](https://doi.org/10.1088/1538-3873/ab006c)
- Habtie, G. R., Das, R., Pandey, R., Ashok, N. M., & Dubovsky, P. A. 2024, *MNRAS*, 527, 1405, doi: [10.1093/mnras/stad3295](https://doi.org/10.1093/mnras/stad3295)
- Hachisu, I., & Kato, M. 2022, *ApJ*, 939, 1, doi: [10.3847/1538-4357/ac9475](https://doi.org/10.3847/1538-4357/ac9475)
- Hillman, Y., Prialnik, D., Kovetz, A., Shara, M. M., & Neill, J. D. 2014, *MNRAS*, 437, 1962, doi: [10.1093/mnras/stt2027](https://doi.org/10.1093/mnras/stt2027)
- Hounsell, R., Bode, M. F., Hick, P. P., et al. 2010, *ApJ*, 724, 480, doi: [10.1088/0004-637X/724/1/480](https://doi.org/10.1088/0004-637X/724/1/480)
- Kato, M., & Hachisu, I. 1994, *ApJ*, 437, 802, doi: [10.1086/175041](https://doi.org/10.1086/175041)
- Kato, M., Saio, H., & Hachisu, I. 2024, *PASJ*, 76, 666, doi: [10.1093/pasj/psae038](https://doi.org/10.1093/pasj/psae038)
- Kloppenborg, B. K. 2023, *Observations from the AAVSO International Database*, <https://www.aavso.org>
- Knigge, C. 2006, *MNRAS*, 373, 484, doi: [10.1111/j.1365-2966.2006.11096.x](https://doi.org/10.1111/j.1365-2966.2006.11096.x)
- Kochanek, C. S., Shappee, B. J., Stanek, K. Z., et al. 2017, *PASP*, 129, 104502, doi: [10.1088/1538-3873/aa80d9](https://doi.org/10.1088/1538-3873/aa80d9)
- König, O., Wilms, J., Arcodia, R., et al. 2022, *Nature*, 605, 248, doi: [10.1038/s41586-022-04635-y](https://doi.org/10.1038/s41586-022-04635-y)
- Law, N. M., Fors, O., Wulfken, P., Ratzloff, J., & Kavanaugh, D. 2014, in *Society of Photo-Optical Instrumentation Engineers (SPIE) Conference Series*, Vol. 9145, *Ground-based and Airborne Telescopes V*, ed. L. M. Stepp, R. Gilmozzi, & H. J. Hall, 91450Z, doi: [10.1117/12.2057031](https://doi.org/10.1117/12.2057031)
- Law, N. M., Corbett, H., Galliher, N. W., et al. 2022, *PASP*, 134, 035003, doi: [10.1088/1538-3873/ac4811](https://doi.org/10.1088/1538-3873/ac4811)
- Li, K.-L., Metzger, B. D., Chomiuk, L., et al. 2017, *Nature Astronomy*, 1, 697, doi: [10.1038/s41550-017-0222-1](https://doi.org/10.1038/s41550-017-0222-1)

- Lu, W., Fuller, J., Quataert, E., & Bonnerot, C. 2023, MNRAS, 519, 1409, doi: [10.1093/mnras/stac3621](https://doi.org/10.1093/mnras/stac3621)
- Masci, F. J., Laher, R. R., Rusholme, B., et al. 2023, arXiv e-prints, arXiv:2305.16279, doi: [10.48550/arXiv.2305.16279](https://doi.org/10.48550/arXiv.2305.16279)
- Metzger, B. D., Hascoët, R., Vurm, I., et al. 2014, MNRAS, 442, 713, doi: [10.1093/mnras/stu844](https://doi.org/10.1093/mnras/stu844)
- Mroz, P., Burdge, K., Roestel, J. v., et al. 2021, The Astronomer's Telegram, 14720, 1
- Mukai, K., & Pretorius, M. L. 2023, MNRAS, 523, 3192, doi: [10.1093/mnras/stad1603](https://doi.org/10.1093/mnras/stad1603)
- Munari, U., Hamsch, F. J., & Frigo, A. 2017, MNRAS, 469, 4341, doi: [10.1093/mnras/stx1116](https://doi.org/10.1093/mnras/stx1116)
- Munari, U., Moretti, S., & Maitan, A. 2020, A&A, 639, L10, doi: [10.1051/0004-6361/202038403](https://doi.org/10.1051/0004-6361/202038403)
- Munari, U., Valisa, P., & Dallaporta, S. 2021, The Astronomer's Telegram, 14704, 1
- Murphy-Glaysher, F. J., Darnley, M. J., Harvey, É. J., et al. 2022, MNRAS, 514, 6183, doi: [10.1093/mnras/stac1577](https://doi.org/10.1093/mnras/stac1577)
- Patterson, J. 1984, ApJS, 54, 443, doi: [10.1086/190940](https://doi.org/10.1086/190940)
- . 1994, PASP, 106, 209, doi: [10.1086/133375](https://doi.org/10.1086/133375)
- Patterson, J., Enestein, J., de Miguel, E., et al. 2022, ApJL, 940, L56, doi: [10.3847/2041-8213/ac9ebe](https://doi.org/10.3847/2041-8213/ac9ebe)
- Pejcha, O., Metzger, B. D., & Tomida, K. 2016, MNRAS, 455, 4351, doi: [10.1093/mnras/stv2592](https://doi.org/10.1093/mnras/stv2592)
- Prialnik, D., Shara, M. M., & Shaviv, G. 1979, A&A, 72, 192
- Quataert, E., Fernández, R., Kasen, D., Klion, H., & Paxton, B. 2016, MNRAS, 458, 1214, doi: [10.1093/mnras/stw365](https://doi.org/10.1093/mnras/stw365)
- Quimby, R. M., Shafter, A. W., & Corbett, H. 2021, Research Notes of the American Astronomical Society, 5, 160, doi: [10.3847/2515-5172/ac14c0](https://doi.org/10.3847/2515-5172/ac14c0)
- Schaefer, B. E. 2021, in American Astronomical Society Meeting Abstracts, Vol. 238, American Astronomical Society Meeting Abstracts, 225.03
- Schaefer, B. E. 2022a, MNRAS, 517, 3640, doi: [10.1093/mnras/stac2089](https://doi.org/10.1093/mnras/stac2089)
- . 2022b, MNRAS, 517, 6150, doi: [10.1093/mnras/stac2900](https://doi.org/10.1093/mnras/stac2900)
- Schaefer, B. E., Landolt, A. U., Linnolt, M., et al. 2013, ApJ, 773, 55, doi: [10.1088/0004-637X/773/1/55](https://doi.org/10.1088/0004-637X/773/1/55)
- Schmidt, R. E., Shugarov, S. Y., & Afonina, M. D. 2021, JAAVSO, 49, 257
- Shappee, B. J., Prieto, J. L., Grupe, D., et al. 2014, ApJ, 788, 48, doi: [10.1088/0004-637X/788/1/48](https://doi.org/10.1088/0004-637X/788/1/48)
- Shen, K. J., & Quataert, E. 2022, ApJ, 938, 31, doi: [10.3847/1538-4357/ac9136](https://doi.org/10.3847/1538-4357/ac9136)
- Shugarov, S., & Afonina, M. 2021, The Astronomer's Telegram, 14835, 1
- Sokolovsky, K. V., Johnson, T. J., Buson, S., et al. 2023, MNRAS, 521, 5453, doi: [10.1093/mnras/stad887](https://doi.org/10.1093/mnras/stad887)
- Starrfield, S., Truran, J. W., Sparks, W. M., Krautter, J., & MacDonald, J. 1990, in IAU Colloq. 122: Physics of Classical Novae, ed. A. Cassatella & R. Viotti, Vol. 369, 306, doi: [10.1007/3-540-53500-4_143](https://doi.org/10.1007/3-540-53500-4_143)
- Strope, R. J., Schaefer, B. E., & Henden, A. A. 2010, AJ, 140, 34, doi: [10.1088/0004-6256/140/1/34](https://doi.org/10.1088/0004-6256/140/1/34)
- Thompson, W. T. 2017, MNRAS, 470, 4061, doi: [10.1093/mnras/stx1552](https://doi.org/10.1093/mnras/stx1552)
- Tonry, J. L., Denneau, L., Flewelling, H., et al. 2018, ApJ, 867, 105, doi: [10.3847/1538-4357/aae386](https://doi.org/10.3847/1538-4357/aae386)
- van Paradijs, J. 1983, in Accretion-Driven Stellar X-ray Sources, ed. W. H. G. Lewin & E. P. J. van den Heuvel, 189–260
- van Paradijs, J., & McClintock, J. E. 1994, A&A, 290, 133
- Wagner, R. M., Woodward, C. E., Starrfield, S., Banerjee, D. P. K., & Evans, A. 2021, The Astronomer's Telegram, 14746, 1
- Woodward, C. E., Banerjee, D. P. K., Geballe, T. R., et al. 2021a, ApJL, 922, L10, doi: [10.3847/2041-8213/ac3518](https://doi.org/10.3847/2041-8213/ac3518)
- Woodward, C. E., Wagner, R. M., Starrfield, S., et al. 2021b, The Astronomer's Telegram, 14723, 1

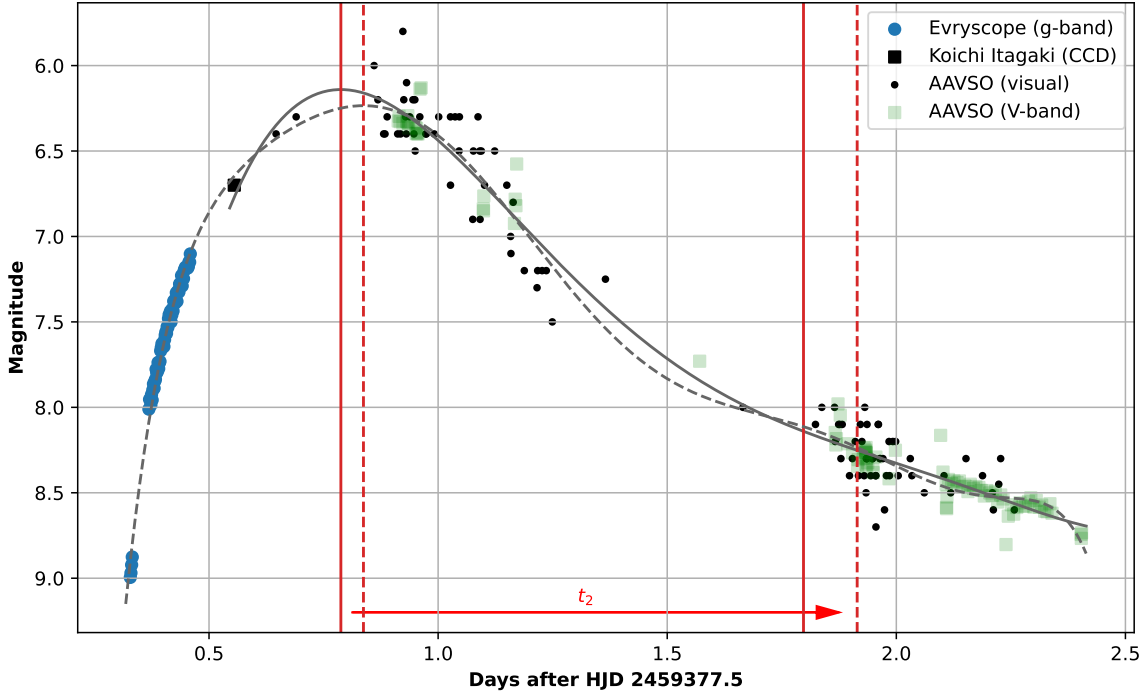


Figure 6. Polynomial fits to the AAVSO data (grey solid curve) and these data supplemented with the faster-rise portion of the Evryscope g -band light curve (dashed grey curve) suggest similar peak magnitudes ($V_{\max} \sim 6.2$ mag) and t_2 times of 1.01 d to 1.08 d.

APPENDIX

A. PEAK MAGNITUDE AND DECLINE RATE OF V1674 HER

Here we use data from the AAVSO (Kloppenborg, B. K. 2023) to determine the peak V-band magnitude of V1674 Her and t_2 , the time it took to fade to 2 mag below this peak. Figure 6 shows visual and V-band measurements of V1674 Her around its peak along with an unfiltered CCD measurement from Koichi Itagaki and the final, faster-rise section of the Evryscope g -band light curve for reference. The solid grey curve is a 6th order polynomial fit excluding the Evryscope data (we assume V -band and visual magnitudes to be equivalent at these phases), and the dashed grey curve is a 10th order polynomial fit *including* the Evryscope data (this further assumes $g - V = 0$). These fits predict peak magnitudes of $V = 6.14$ mag at $t_{\text{ref}} + 0.7878$ d and $V = 6.23$ mag at $t_{\text{ref}} + 0.8371$ d, respectively. The t_2 values for these fits are 1.01 d and 1.08 d, respectively. We thus conclude that V1674 Her reached a peak V-band magnitude of $V = 6.19 \pm 0.05$ and declined by 2 magnitudes in 1.04 ± 0.03 d.

Table 1. ASAS-SN Photometry

HJD	Flux	σ_{Flux}	g	σ_g	Limit
	mJy	mJy	mag	mag	mag
(1)	(2)	(3)	(4)	(5)	(6)
2459377.6944	0.557	0.137	17.035	0.267	16.810
2459377.6956	1.161	0.153	16.238	0.143	16.693
2459377.6968	0.978	0.143	16.424	0.159	16.762

NOTE—HJD values mark the beginning of the 90 s exposures. Limits are 5σ .

Table 2. Evryscope Photometry

HJD	Flux	σ_{Flux}	g	σ_g	Limit
	mJy	mJy	mag	mag	mag
(1)	(2)	(3)	(4)	(5)	(6)
2459377.7527	2.52	1.08	15.064
2459377.7541	2.22	1.08	15.094
2459377.7556	2.57	1.07	15.133
2459377.7570	2.61	1.11	15.149
2459377.7584	4.19	1.11	14.844	0.288	15.114
2459377.7598	3.64	1.10	14.997	0.328	15.140
2459377.7612	4.72	1.09	14.715	0.250	15.128
2459377.7627	3.30	1.08	15.104	0.356	15.123
2459377.7641	4.96	1.09	14.662	0.238	15.203
2459377.7655	3.67	1.05	14.988	0.310	15.092
2459377.7670	5.28	1.07	14.594	0.220	15.088
2459377.7684	5.38	1.08	14.573	0.217	15.121
2459377.7698	4.54	1.08	14.757	0.258	15.086
2459377.7712	4.93	1.10	14.667	0.242	15.097
2459377.7726	7.62	1.11	14.195	0.158	15.147
2459377.7741	5.50	1.11	14.548	0.218	15.137
2459377.7755	3.74	1.09	14.967	0.316	15.087
2459377.7769	1.17	1.06	15.144
2459377.7784	4.50	1.06	14.767	0.256	15.243
2459377.7798	4.67	1.06	14.727	0.247	15.129
2459377.7812	10.86	1.07	13.811	0.107	15.162
2459377.7826	19.12	1.11	13.196	0.063	15.121
2459377.7840	34.61	1.17	12.552	0.037	15.214
2459377.7855	53.06	1.21	12.088	0.025	15.189
2459377.7869	74.93	1.27	11.713	0.018	15.212
2459377.7883	101.63	1.35	11.382	0.014	15.227
2459377.7897	124.83	1.39	11.159	0.012	15.190
2459377.7912	157.23	1.45	10.909	0.010	15.205
2459377.7926	178.65	1.48	10.770	0.009	15.254
2459377.7940	206.70	1.53	10.612	0.008	15.211
2459377.7954	233.40	1.56	10.480	0.007	15.155
2459377.7969	268.33	1.61	10.328	0.007	15.172
2459377.7983	290.98	1.66	10.240	0.006	15.161
2459377.7997	322.49	1.73	10.129	0.006	15.201
2459377.8011	351.36	1.78	10.036	0.006	15.163
2459377.8026	372.68	1.83	9.972	0.005	15.218
2459377.8040	399.69	1.88	9.896	0.005	15.244
2459377.8054	430.99	1.92	9.814	0.005	15.168
2459377.8068	456.27	2.01	9.752	0.005	15.167
2459377.8083	484.00	2.07	9.688	0.005	15.156
2459377.8097	511.76	2.11	9.627	0.004	15.249
2459377.8111	545.85	2.16	9.557	0.004	15.182
2459377.8125	574.85	2.32	9.501	0.004	15.177
2459377.8140	605.42	2.36	9.445	0.004	15.261
2459377.8154	640.89	2.40	9.383	0.004	15.215
2459377.8168	665.59	2.43	9.342	0.004	15.214
2459377.8183	702.12	2.55	9.284	0.004	15.275

Table 2 *continued*

Table 2 (*continued*)

HJD	Flux	σ_{Flux}	g	σ_g	Limit
	mJy	mJy	mag	mag	mag
(1)	(2)	(3)	(4)	(5)	(6)
2459377.8197	730.93	2.65	9.240	0.004	15.151
2459377.8211	753.47	2.75	9.207	0.004	15.174
2459377.8225	785.42	2.78	9.162	0.004	15.155
2459377.8239	803.56	2.79	9.137	0.004	15.128
2459377.8254	841.10	2.83	9.088	0.004	15.236
2459377.8268	865.52	3.04	9.057	0.004	15.217
2459377.8282	916.09	2.99	8.995	0.004	15.208
2459377.8296	938.54	3.10	8.969	0.004	15.191
2459377.8311	980.05	3.38	8.922	0.004	15.199
2459377.8325	1022.46	3.44	8.876	0.004	15.168
2459377.8688	2268.52	8.77	8.011	0.004	15.795
2459377.8702	2390.97	10.16	7.954	0.005	15.792
2459377.8716	2389.91	9.52	7.954	0.004	15.871
2459377.8731	2319.60	9.28	7.986	0.004	15.863
2459377.8745	2454.78	9.72	7.925	0.004	15.820
2459377.8759	2383.21	9.20	7.957	0.004	15.751
2459377.8773	2516.92	10.03	7.898	0.004	15.800
2459377.8788	2599.60	10.29	7.863	0.004	15.764
2459377.8802	2538.88	9.46	7.888	0.004	15.792
2459377.8816	2635.60	10.32	7.848	0.004	15.843
2459377.8830	2663.69	10.04	7.836	0.004	15.791
2459377.8845	2812.66	10.75	7.777	0.004	15.803
2459377.8859	2758.41	10.33	7.798	0.004	15.825
2459377.8873	2778.49	10.72	7.790	0.004	15.846
2459377.8887	2917.14	11.76	7.738	0.004	15.822
2459377.8902	2821.56	9.73	7.774	0.004	15.718
2459377.8916	2911.41	10.91	7.740	0.004	15.699
2459377.8930	2934.27	10.35	7.731	0.004	15.788
2459377.8944	3106.28	11.32	7.669	0.004	15.786
2459377.8959	3163.45	11.56	7.650	0.004	15.738
2459377.8973	3229.46	11.89	7.627	0.004	15.775
2459377.8987	3166.37	11.06	7.649	0.004	15.784
2459377.9001	3179.87	11.14	7.644	0.004	15.764
2459377.9016	3178.30	11.18	7.645	0.004	15.749
2459377.9030	3297.47	11.84	7.605	0.004	15.739
2459377.9044	3382.01	12.01	7.577	0.004	15.788
2459377.9058	3441.23	12.15	7.558	0.004	15.740
2459377.9073	3410.75	11.96	7.568	0.004	15.801
2459377.9087	3538.72	12.58	7.528	0.004	15.795
2459377.9101	3521.68	12.21	7.533	0.004	15.834
2459377.9115	3696.03	12.62	7.481	0.004	15.825
2459377.9130	3775.92	12.65	7.457	0.004	15.697
2459377.9144	3767.51	12.83	7.460	0.004	15.748
2459377.9158	3847.25	12.73	7.437	0.004	15.690
2459377.9172	3631.40	11.72	7.500	0.004	15.740
2459377.9187	3764.39	11.78	7.461	0.003	15.745
2459377.9201	3897.85	13.42	7.423	0.004	15.778
2459377.9215	3849.65	12.33	7.436	0.003	15.673
2459377.9229	4062.71	13.83	7.378	0.004	15.753
2459377.9244	4045.05	12.79	7.383	0.003	15.780

Table 2 *continued*

Table 2 (*continued*)

HJD	Flux	σ_{Flux}	g	σ_g	Limit
	mJy	mJy	mag	mag	mag
(1)	(2)	(3)	(4)	(5)	(6)
2459377.9258	4013.44	13.00	7.391	0.004	15.726
2459377.9272	4117.75	13.59	7.363	0.004	15.753
2459377.9286	4248.82	13.87	7.329	0.004	15.778
2459377.9301	4055.42	12.23	7.380	0.003	15.805
2459377.9315	4265.78	13.43	7.325	0.003	15.802
2459377.9329	4301.47	13.43	7.316	0.003	15.699
2459377.9343	4265.11	12.93	7.325	0.003	15.763
2459377.9358	4454.89	13.70	7.278	0.003	15.796
2459377.9372	4459.74	13.14	7.277	0.003	15.698
2459377.9386	4414.00	12.90	7.288	0.003	15.724
2459377.9400	4661.62	14.22	7.229	0.003	15.703
2459377.9415	4407.32	13.04	7.290	0.003	15.772
2459377.9429	4588.03	13.48	7.246	0.003	15.765
2459377.9443	4584.41	13.39	7.247	0.003	15.800
2459377.9457	4785.28	14.14	7.200	0.003	15.781
2459377.9472	4832.53	14.57	7.190	0.003	15.739
2459377.9486	4876.00	13.70	7.180	0.003	15.703
2459377.9535	4852.54	12.50	7.185	0.003	15.462
2459377.9549	4894.31	12.61	7.176	0.003	15.460
2459377.9563	5018.83	12.87	7.148	0.003	15.439
2459377.9577	5010.01	12.74	7.150	0.003	15.428
2459377.9591	5237.22	13.53	7.102	0.003	15.408

NOTE—HJD values mark the midpoint of the 120 s exposures. Uncertainties are statistical only. Limits are for 50% completeness.